Mineralium Deposita (2023) 58:1263–1278
https://doi.org/10.1007/s00126-023-01178-8

ARTICLE

Molybdenum cycling in Andean-type subduction and metallogenic implications

Wei Mao[1] · Hong Zhong[1,2] · Jiehua Yang[1] · Liang Liu[1] · Yazhou Fu[1] · Xingchun Zhang[1] · Jie Li[3] · Le Zhang[3] · Haifeng Fan[1] · Yanwen Tang[1] · Xiaocui Chen[4]

Received: 15 December 2022 / Accepted: 17 April 2023 / Published online: 1 May 2023

Abstract

We have conducted Mo isotope analyses of granites and related hydrothermal molybdenite from six Sn-W deposits in the western belt of the Southeast Asian Tin Province (Myanmar and Yunnan, China). Our data show that tin granites have notably heavier Mo isotope compositions (avg. δ^{98}Mo = 0.44 ‰) than arc lavas (avg. δ^{98}Mo = −0.12 ‰). The lack of systematic variation of Mo isotope composition with SiO_2, Differentiation Index, Rb/Sr, and Zr/Hf values of the studied tin granites suggests there was no Mo isotope fractionation caused by fractional crystallization of the reduced magma. We infer that the elevated Mo isotope compositions in tin granites are mainly inherited from reduced sedimentary sources with black shales (avg. δ^{98}Mo = 0.44 ‰). We also observed remarkable Mo isotope fractionation during the magmatic-hydrothermal transition. The preferential incorporation of Mo^{4+} and isotopically light Mo into magmatic sulfides and partitioning of Mo^{6+} and heavy Mo isotopes into hydrothermal fluids account for significant fluid-melt fractionation of Mo isotopes during fluid exsolution from the reduced melt. The elevated Mo isotope composition in hydrothermal molybdenite from granite-related Sn-W deposits compared to that of porphyry Cu–Mo deposits derives from both the notably heavy Mo isotope signature of the reduced sedimentary sources and fluid-melt fractionation of Mo isotopes during the magmatic-hydrothermal transition. The sequestration of Mo during crystallization of reduced melt and the low Mo precipitation efficiency in the hydrothermal evolution prevents the formation of economic Mo mineralization in reduced magmatic-hydrothermal systems. Combined with published data from different Mo sinks, we propose a Mo cycling and isotope fractionation model for arc and back-arc systems of Andean-type subduction settings.

Keywords Sn-W deposit · Mo isotope · Isotope fractionation · Andean-type subduction · Southeast Asia

Introduction

Molybdenum released during continental weathering is transported to the oceans and redistributed into oxic and reduced sinks with complementary isotopic composition (Anbar 2004; Arnold et al. 2004). Oxic pelagic sediments formed in open oceans have distinctively low Mo isotope signatures owing to the adsorption of light Mo isotopes by Mn-oxides (Barling et al. 2001; Siebert et al. 2003; Barling and Anbar 2004). In contrast, reduced sediments (e.g., organic-rich mudstone) deposited on continental margins in euxinic and suboxic basins may record the heavy Mo signature of seawater due to near complete Mo scavenging under reducing conditions (Barling et al. 2001; Arnold et al. 2004). Despite the limited cover of the present-day seafloor by reduced sediments (~0.05 to 0.10 %), such sediments account for the removal of 6 to 15 % Mo from seawater (Kendall et al. 2017).

Editorial handling: B. Lehmann

✉ Wei Mao
maowei@mail.gyig.ac.cn

[1] State Key Laboratory of Ore Deposit Geochemistry, Institute of Geochemistry, Chinese Academy of Sciences, Guiyang 550081, China

[2] University of Chinese Academy of Sciences, Beijing 100049, China

[3] State Key Laboratory of Isotope Geochemistry, Guangzhou Institute of Geochemistry, Chinese Academy of Sciences, Guangzhou 510640, China

[4] Guizhou Institute of Technology, Guiyang 550003, China

Molybdenum is mobile and redistributed during slab subduction and dehydration, depending on the redox conditions (Bali et al. 2012; Skora et al., 2017). The isotopically light Mo is preferentially incorporated into secondary minerals like rutile (Bali et al. 2012; Freymuth et al. 2015; Skora et al. 2017; Chen et al. 2019; Ahmad et al. 2021; Li HY et al. 2021a). The heavy Mo isotopes are enriched in aqueous fluids released by slab dehydration, leading to metasomatism of the mantle wedge and accounting for the relatively higher $\delta^{98/95}Mo_{NIST3134}$ (herein $\delta^{98}Mo$) in arc lavas compared to the depleted mantle (Freymuth et al. 2015; König et al. 2016; Villalobos-Orchard et al. 2020). Cycling of black shales deposited on oceanic crust in the subduction setting would produce arc lavas with notably heavier Mo isotope compositions than normal arc lavas (Freymuth et al. 2016; Skora et al. 2017). If oxic arc magma emplaced in the upper continental crust achieves water saturation, aqueous fluids extract metals from the magma to form porphyry Cu-Mo deposits (Lowell and Guilbert 1970; Sillitoe 1973, 2010). Significant Mo isotope fractionation has been identified during molybdenite precipitation from hydrothermal fluids in porphyry deposits (Hannah et al. 2007; Greber et al. 2011, 2014; Shafiei et al. 2014).

Black shales deposited on continental margins are less likely to be subducted (Tourtelot 1979), but they can be cycled if the sedimentary crust is formed in extensional settings and then melted by underplating (Jiménez and López-Velásquez 2008; Sato 2012). Partial melting of metasedimentary sequences with black shales in Andean-type subduction was likely responsible for the large-scale reduced magmatism and hydrothermal events that produced the world-class tin provinces in Southeast Asia, South China, and the Central Andes (Lehmann 1982, 1990; Lehmann et al. 1990; Mitchell 2018; Zhao et al. 2022). Many Mo isotope data have been obtained on reduced sediments, especially black shales (e.g., Ye et al. 2021), however, magma derived from reduced sediments and its hydrothermal products rarely attracted attention (Yao et al. 2016; Segato 2018). The very limited molybdenite Mo isotope data on granite-related Sn–W deposits (avg. $\delta^{98}Mo = 0.93$ ‰, $n = 25$; Malinovsky et al. 2007; Breillat et al. 2016; Yao et al. 2016; Segato 2018) are notably heavier than those on porphyry deposits, but the mechanism for the elevated $\delta^{98}Mo$ is unclear.

As isotopic fractionation is governed by bond energy, coordination, and valence state of atoms (Schauble 2004), more significant Mo isotope fractionation is expected in reduced magmatic-hydrothermal systems where Mo^{6+} and Mo^{4+} species coexist (O'Neill and Eggins 2002; Kaufmann et al. 2021). Although Mo is subeconomic in typical granite-related Sn–W deposits, it is potentially an important indicator of mass flow in reduced environments. In this study, we analyze Mo isotopes of tin granites and related hydrothermal molybdenite from six Sn–W deposits from the western belt of the Southeast Asian Tin Province, compile Mo isotope data of variable sinks, and discuss Mo cycling and isotope fractionation in arc and back-arc systems of Andean-type subduction settings and related mineralization.

Geological background

The Southeast Asian Tin Province accounts for 40~45 % of the global historic tin production (Mitchell 1977, 1979; Schwartz et al. 1995; Lehmann 2021). Based on the spatial distribution, tectonic setting, and mineralization ages, tin mineralization in the Southeast Asian Tin province was divided into the Eastern, Central, and Western belts (Fig. 1; Mitchell, 1977, 1979, 2018; Mitchell and Garson, 1981; Cobbing et al., 1986; Schwartz et al., 1995; Sone and Metcalfe, 2008). The Western tin belt, extending from western Yunnan through Myanmar to Phuket Island of Thailand, hosts numerous Sn–W deposits related to granites with characteristically low oxidation state (ilmenite-series granites; Fig. 1; Ishihara 1977; Lehmann 1990; Mitchell 2018). Most of these tin granites are peraluminous biotite, biotite-muscovite, or muscovite-tourmaline granites (Ishihara et al. 1980; Lehmann and Mahawat 1989; Chen et al. 2015; Gardiner et al. 2016a, b; Mitchell 2018). The reduced granite magmatism and related Sn-W deposits were mainly formed during the subduction of the Neo-Tethys oceanic slab from the Late Cretaceous to the Eocene (Mitchell 1977, 1979; Mao et al. 2020, 2022; Zhang et al. 2021). The Wuntho-Popa Arc and related porphyry-style Cu mineralization in western Myanmar were subparallel to the Western tin belt before the Late Cenozoic displacement along the Sagaing fault (Mitchell 1993). Therefore, the tectonic setting of these two belts with contrasting magmatic and mineralization styles was recognized as Andean-type subduction (Mitchell 1986; Gardiner et al. 2015).

Sn-W deposits in the Western tin belt are mainly distributed in the Slate Belt in Myanmar and its equivalent in western Yunnan, China (Fig. 1). The Slate Belt is a thick succession of argillite, slate, and quartzite overlain by diamictite formed on the margin of Gondwana in the Carboniferous (Mitchell 2018). Our study mainly focuses on six Sn-W deposits from Myanmar and western Yunnan (Fig. 1). The Kuntabin deposit in southern Myanmar recorded the earliest Sn-W mineralization (~88 Ma) related to the subduction of the Neo-Tethys (Mao et al. 2020). The Xiaolonghe and Dasongpo deposits (~72 Ma) in western Yunnan were formed during the continuous subduction of the Neo-Tethys (Chen et al. 2014, 2015). The Hermyingyi (~61 Ma) and Bwabin (~63 Ma) deposits, hosted in one of the most productive regions in Myanmar (the Dawei area), were related to the roll-back of the Neo-Tethys oceanic slab (Li et al. 2018). The India and Eurasia collision initiated in Tibet at ~65-63 Ma, then the

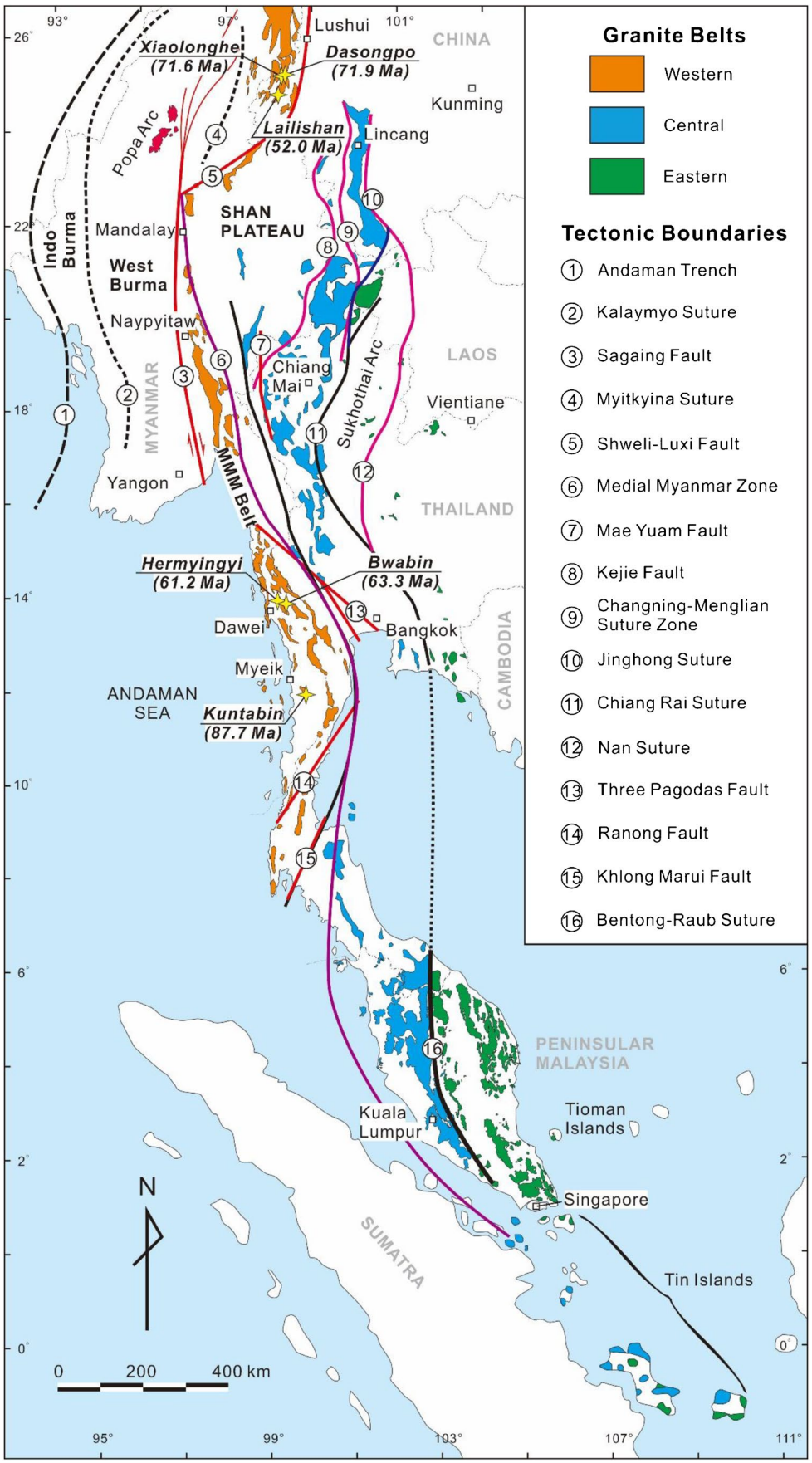

Fig. 1 Simplified map showing granite belts, tectonic boundaries, and the studied Sn-W deposits in the Southeast Asian Tin Province. Modified after Mitchell (1977, 2018), Cobbing et al. (1986), Sone and Metcalfe (2008), Mitchell et al. (2015), Searle et al. (2016), and Cong et al. (2021). Numbers in brackets are cassiterite U-Pb ages of Sn-W mineralization from Chen et al. (2014) and Mao et al. (2020, 2022)

Neo-Tethys Ocean was closed diachronously both to the west and east (Searle et al. 2007; Royden et al. 2008; Ding et al. 2014). The Lailishan deposit (~52 Ma) formed in a post-collisional setting after the collision reached western Yunnan (Chen et al. 2014, 2015).

The tin granites from the Lailishan, Xiaolonghe, and Dasongpo deposits in Yunnan are medium- to coarse-grained biotite granites, consisting of ~20 to 30 % quartz, ~60 to 65 % feldspar, ~10 % biotite, and minor muscovite (Figs. 2A, B, C). The Kuntabin granite in Myanmar is a medium- to coarse-grained two-mica granite, consisting of ~30 % quartz, ~50 % feldspar, ~10 % biotite, and ~10 % muscovite (Fig. 2D). The Hermyingyi and Bwabin granites in Myanmar are medium- to fine-grained muscovite granites, containing

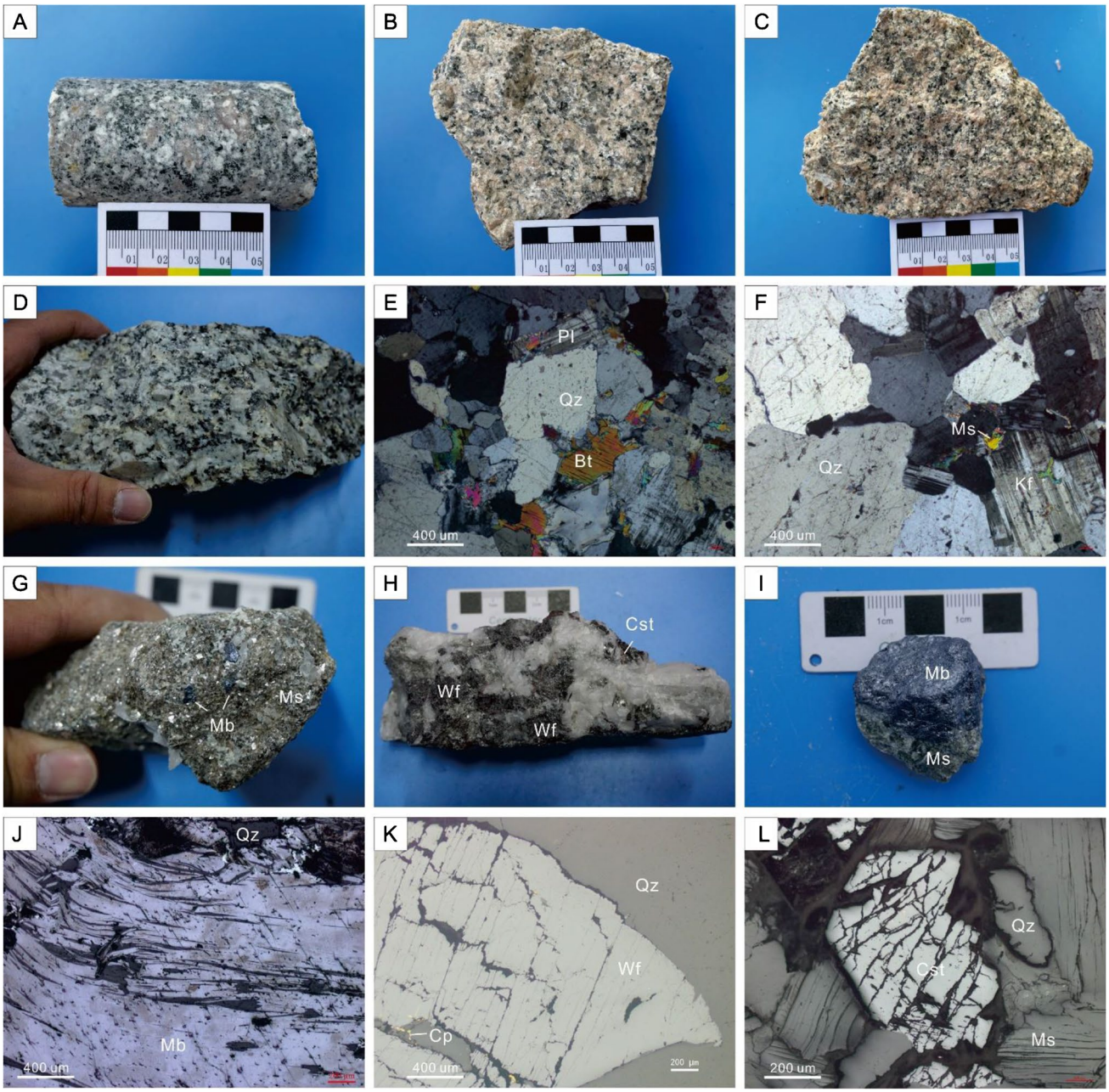

Fig. 2 **A–D** Least-altered granite samples. **E**, **F** Cross-polarized images of granites. **G–I** Hydrothermal veins with cassiterite-wolframite-sulfide mineralization. **J–L** Reflected-light images of cassiterite, wolframite, and sulfides. Images A, B, and C are from the Lailishan, Xiaolonghe, and Dasongpo deposits, respectively. Images D, G, and J are from the Kuntabin deposit. Images E, H, and K are from the Hermyingyi deposit. Images F, I, and L are from the Bwabin deposit. Abbreviations: Bt = biotite, Cp = chalcopyrite, Cst = cassiterite, Kf = K-feldspar, Mb = molybdenite, Ms = muscovite, Pl = plagioclase, Qz = quartz, Wf = wolframite

~30 % quartz, ~50 % feldspar, ~15 to 18 % muscovite, and minor biotite (Figs. 2E, F). Opaque minerals in these granites include ilmenite and hydrothermal pyrite, chalcopyrite, pyrrhotite, sphalerite, galena, and arsenopyrite (Figs. 2J, K, L).

Tin and tungsten ores in these deposits generally occur near the granite boundary. Intensive greisenization occurred in granite on both sides of quartz veins with alteration to muscovite and quartz. The width of cassiterite and wolframite-bearing veins varies from centimeters to over 2 m. Cassiterite and wolframite are the dominant ore minerals. There is only a trace amount of molybdenite in Kuntabin and Hermyingyi, but large aggregates of molybdenite have been sampled in the Bwabin deposit, while no molybdenite could be collected from the Lailishan, Xiaolonghe, and Dasongpo deposits (Figs. 2G, H, I).

Methods

Thirty-five least altered granite samples from the six Sn-W deposits in Myanmar and western Yunnan have been ground to <200 mesh for analysis. A total of 21 molybdenite samples from the Kuntabin, Hermyingyi, and Bwabin deposits have been hand-picked and purified under the microscope after crushing of hydrothermal vein samples. The molybdenite samples were then ground to <200 mesh for further analysis.

Whole-rock major and trace element analyses

Major and trace element analyses of bulk-granite samples were conducted at the State Key Laboratory of Ore Deposit Geochemistry, Institute of Geochemistry, Chinese Academy of Sciences (SKLODG, IGCAS), Guiyang. The major elements were determined with a Thermo Fisher ARL Perform'X 4200 X-ray fluorescence spectrometer. The mixtures of granite powders (0.4 g) with $Li_2B_4O_7$ (8.0 g) were fused at 1100°C and cast into glass discs for analysis. The analytical precision is generally better than ±5 %. The trace elements were determined with a Plasma Quant-MS Elite ICP-MS. Granite powders (50 mg) were digested in high-pressure Teflon bombs with a HF-HNO_3 mixture for 48 h at 190°C, and then evaporated and dissolved in 2 % HNO_3. An internal Rh standard was used to monitor signal drift during analysis. The international standard AGV-2 was used to monitor the analytical precision and accuracy. The analytical precisions are generally better than ±10 %. Detailed analytical procedures are described by Qi et al. (2000). The Differentiation Index was calculated following the method of Thornton and Tuttle (1960).

Zircon and mica LA-ICP-MS trace element analysis

Zircon and mica LA-ICP-MS trace element analyses were conducted at SKLODG, IGCAS. The analytical system is composed of a *GeoLas Pro* 193 nm ArF excimer laser ablation system and an Agilent 7500× ICP-MS instrument. Helium was used as carrier gas which was mixed with argon via a T-connector before entering the ICP-MS. The zircon analysis was carried out with a laser energy density of 5 J/cm^2, a repetition rate of 5 Hz, and a spot size of 32 µm. The mica analysis was carried out with a laser energy density of 4.5 J/cm^2, a repetition rate of 6 Hz, and a spot size of 44 µm. The standard NIST 610 was used as the external standard. Zirconium (489,700 ppm) was used as the internal standard for trace element calibration in zircon. Aluminum analyzed by Electro Probe Micro-Analysis was used as the internal standard for trace element calibration in mica. Data reduction was carried out by the ICPMSDataCal program (Liu et al. 2008, 2010). Ti-in-zircon temperature and oxygen fugacity of magma were calculated by zircon trace elements using the method of Loucks et al. (2020).

Zircon Hf isotope analysis

Zircon Hf isotope analyses were conducted at the SKLODG, IGCAS. The analytical system is composed of a RESOlution S-155 193nm excimer laser ablation and a Nu Plasma III MC-ICP-MS. A laser energy density of 6 J/cm^2, a repetition of 6 Hz, and a spot size of 60 µm were used for analysis. Detailed analytical procedures were reported by Wu et al. (2006). The $\varepsilon_{Hf}(t)$ values were calculated relative to the chondritic reservoir, with the decay constant of 1.867 ± 0.00810^{-11} y^{-1} (Scherer et al. 2001). The two-stage Hf model ages (T_{DM2}) were calculated assuming a mean $^{176}Lu/^{177}Hf$ value of 0.015 for the average continental crust (Griffin et al. 2002). Correction for isobaric interference of ^{176}Lu and ^{176}Yb on ^{176}Hf was conducted using $^{176}Yb/^{173}Yb = 0.7962$ and $^{176}Lu/^{175}Lu = 0.02655$ with an exponential-law mass bias correction assuming a $^{173}Yb/^{171}Yb$ ratio of 1.129197 (Vervoort et al. 2004). Zircon Penglai was used as the reference material and returned the weighted mean $^{176}Hf/^{177}Hf$ results of 0.282907 ± 0.000013, identical to the recommended value of 0.282906 ± 0.000010 (Li et al. 2010).

Mo isotope analysis

The Mo isotope composition of granite and molybdenite samples was measured at the State Key Laboratory of Isotope Geochemistry, Guangzhou Institute of Geochemistry, Chinese Academy of Sciences in Guangzhou, using the double-spike method described in Li et al. (2014). Around 50 mg of granite powder were precisely weighed and placed in individual 15 mL PFA (perfluoroalkoxy alkane) beakers. A ^{97}Mo-^{98}Mo double-spike solution was added to the samples. The samples were dissolved with 8 mL of a 1:2 mixture of HNO_3 and HF at 140°C for 3 days. After digestion, the solution was dried at 120°C and then dissolved with 4

mL of 1 mol/L HNO_3/0.3 mol/L HF for column separation. Molybdenum was separated and purified from the solution following the protocol in Li et al. (2014). Sample division was processed for the molybdenite powders, and then ~5 mg molybdenite powders of each sample were weighted and digested in the Teflon containers with 1.5 mL HF and 1.5 mL HNO_3 at 180°C for 2 days. The solutions were then evaporated to dryness to remove HF completely, and then diluted by 0.5 mL HNO_3. A ^{97}Mo-^{98}Mo double-spike solution was added to the sample solutions 1 day before measurement for the solutions to reach equilibrium. Mo isotopic ratios were then determined with a Thermo-Fisher Scientific Neptune Plus multiple-collector inductively coupled plasma mass spectrometry.

The isotopic composition of Mo is expressed as δ^{98}Mo relative to the NIST 3134 standard as $\delta^{98/95}$Mo (‰) = [(^{98}Mo/^{95}Mo$_{sample}$)/(^{98}Mo/^{95}Mo$_{NIST3134}$)-1]×1000 (Li et al. 2014). The NIST SRM 3134 standard solution and reference materials, including IAPSO (seawater), GBW07316 (offshore marine sediment), and AGV-2 (Andesite), were measured along with the samples. The IAPSO standard yielded a δ^{98}Mo$_{NIST}$ value of 2.05 ± 0.04 ‰, the GBW07316 reference material yielded a δ^{98}Mo$_{NIST}$ value of -0.72 ± 0.05 ‰, and the AGV-2 standard yielded a δ^{98}Mo$_{NIST}$ value of −0.18 ± 0.05 ‰; all these values agree within error with previously published values (Li et al. 2014; Yang et al. 2015, 2017; Willbold et al. 2016). The procedural blank for Mo analysis was ~0.61 ± 0.25 ng, far less than total Mo in the samples. Where necessary, literature Mo isotope data in this study have been re-calculated to δ^{98}Mo = 0 ‰ for NIST SRM 3134 for consistency, following the proposed intercalibration in Goldberg et al. (2013).

Results

All granite samples have notably high SiO_2 contents and Differentiation Index values, with SiO_2 ranging from 72.0 to 77.7 wt% and DI ranging from 84.5 to 97.0 (Table 1). The Rb/Sr and Zr/Hf ratios of the granites are distinctive among different deposits but are generally homogeneous in each deposit (Fig. 3). Oxygen fugacity (logfO_2) calculated from zircon trace elements ranges from ΔFMQ-3.5 to ΔFMQ-1.4 (avg. = ΔFMQ-2.3) for Kuntabin, from ΔFMQ-1.8 to ΔFMQ-0.4 (avg. = ΔFMQ-1.2) for Hermyingyi, and from ΔFMQ-1.4 to ΔFMQ+1.0 (avg. = ΔFMQ+0.1) for Bwabin (ESM, Table 1a; FMQ is the Fayalite-Magnetite-Quartz buffer). The calculated zircon $\varepsilon_{Hf}(t)$ values range from −14.5 to −10.7 (avg. = −12.8) for Hermyingyi and from −17.3 to −12.4 (avg. = −13.9) for Bwabin (ESM Table 1b). Mo contents in mica range from 0.05 ppm to 0.61 ppm (avg. = 0.29 ppm) for the Kuntabin granite, from 0.01 ppm to 0.61 ppm (avg. = 0.24 ppm) for the Hermyingyi granite, and from 0.04 ppm to 0.21 ppm (avg. = 0.09 ppm) for the Bwabin granite (Table 2).

Five bulk-rock granite samples from the Kuntabin deposit have Mo contents of 0.62 ppm to 3.47 ppm (avg. = 1.43 ppm) and δ^{98}Mo values of −0.10 to 0.19 ‰ (avg. = 0.07 ‰; Fig. 4; Table 1). Seven molybdenite samples from Kuntabin have δ^{98}Mo values of 1.30 to 1.94 ‰ (avg. = 1.58 ‰; Table 3). Six granite samples from the Hermyingyi deposit have Mo contents of 0.42 to 5.67 ppm (avg. = 2.83 ppm) and δ^{98}Mo values of 0.90 to 1.06 ‰ (avg. = 1.00 ‰). Five molybdenite samples from Hermyingyi have δ^{98}Mo values of 1.35 to 2.08 ‰ (avg. = 1.65 ‰). Five bulk-rock granite samples from the Bwabin deposit have Mo contents of 0.51 ppm to 6.33 ppm (avg. = 2.54 ppm) and δ^{98}Mo values of −0.31 to 0.16 ‰ (avg. = −0.04 ‰). Nine molybdenite samples from Bwabin have δ^{98}Mo values of −0.36 to 0.44 ‰ (avg. = 0.00 ‰).

Three bulk-rock granite samples from the Lailishan deposit have Mo contents of 0.35 to 3.30 ppm (avg. = 1.40 ppm) and δ^{98}Mo values of 0.17 to 0.44 ‰ (avg. = 0.29 ‰). Eight bulk-rock granite samples from the Xiaolonghe deposit have Mo contents of 0.87 to 20.5 ppm (avg. = 6.25 ppm) and δ^{98}Mo values of 0.04 to 0.70 ‰ (avg. = 0.36 ‰). Seven bulk-rock granite samples from the Dasongpo deposit have Mo contents of 0.47 to 9.45 ppm (avg. = 3.00 ppm) and δ^{98}Mo values of 0.61 to 1.10 ‰ (avg. = 0.78 ‰; Fig. 4; Table 1).

The Mo isotope compositions of the studied tin granites span a wide range from −0.3 to 1.1 ‰, with an average of 0.44 ‰, notably heavier than arc lavas (avg. = −0.12 ‰; Freymuth et al. 2015; König et al. 2016; Villalobos-Orchard et al. 2020; Ahmad et al. 2021; Li HY et al. 2021a; Li X et al. 2021b), and equal to the average of black shales (0.44 ‰; Ye et al. 2021 and references therein). The Mo isotope compositions of the studied molybdenite span a wide range from −0.36 to 2.08 ‰, with an average of 0.92 ‰, consistent with the average of molybdenite analyzed in other Sn-W deposits (avg. =0.93; Malinovsky et al. 2007; Breillat et al. 2016; Yao et al. 2016; Segato 2018).

Previous studies revealed that molybdenite Mo isotope variations may be significant in individual deposits (Kendall et al. 2009, 2017; Mathur et al. 2010; Greber et al. 2011, 2014; Shafiei et al. 2014; Breillat et al. 2016; Segato 2018). For example, the ranges of molybdenite δ^{98}Mo values are ~0.76 ‰ (n = 14) for the Yulong porphyry Cu–Mo deposit, ~1.27 ‰ (n = 20) for the Qulong porphyry Cu–Mo deposit, and ~0.88 ‰ (n = 42) for the Questa porphyry Mo deposit (Greber et al. 2014; Li et al. 2019a, 2019b; Chang et al. 2020). The ranges of molybdenite δ^{98}Mo values are ~0.64 ‰ (n = 7) for Kuntabin, ~0.73 ‰ for Hermyingyi (n = 5), and ~0.80 ‰ for Bwabin (n = 9). Although the number of our analyses in individual deposits is small compared to studies in the above porphyry deposits, there is no correlation between the ranges of δ^{98}Mo values and a number of analyses neither in our data nor in previous studies. Therefore, we infer that our analytical results are generally representative of the Mo isotope variations in individual deposits.

Table 1 SiO_2, Differentiation Index, Rb/Sr, Zr/Hf, $\delta^{98}Mo$ and Mo contents of tin granites from Sn–W deposits in the Western belt of the Southeast Asian Tin Province

Deposit	Sample	SiO_2 (wt. %)	DI	Rb/Sr	Zr/Hf	Mo content (ppm)	$\delta^{98}Mo_{NIST}$ (‰)	2σ
Kuntabin, Myanmar	KTB-Gr-1	73.3	90.7	10.8	32.9	3.47	−0.10	0.05
	KTB-Gr-2	73.5	91.2	12.2	34.2	0.93	0.12	0.06
	KTB-Gr-3	73.6	91.2	12.1	33.2	1.17	0.08	0.05
	KTB-Gr-4	73.3	90.1	10.7	34.6	0.62	0.19	0.03
	KTB-Gr-5	72.0	89.4	11.6	34.4	0.96	0.07	0.04
Hermyingyi, Myanmar	HMY-Gr-1	76.4	94.1	283.8	12.8	5.67	1.02	0.05
	HMY-Gr-2	75.1	92.5	213.6	11.2	2.36	1.03	0.06
	HMY-Gr-3	76.1	93.1	179.2	12.1	4.22	1.06	0.05
	HMY-Gr-4	74.6	90.1	217.9	17.6	0.87	0.90	0.04
	HMY-Gr-5	76.1	93.7	191.7	10.5	3.45	1.03	0.05
	HMY-Gr-6	73.6	84.5	671.0	12.3	0.42	0.93	0.05
Bwabin, Myanmar	BB-Gr-1	76.9	95.9	254.4	10.9	6.33	−0.08	0.05
	BB-Gr-2	76.6	95.9	250.0	10.8	2.23	0.07	0.07
	BB-Gr-3	77.7	96.1	247.8	10.7	4.53	−0.15	0.05
	BB-Gr-4	77.2	92.2	316.7	10.8	1.10	−0.31	0.05
	BB-Gr-5	75.8	95.2	160.4	10.9	0.51	0.10	0.06
	BB-Gr-6	77.5	94.7	266.4	10.7	0.53	0.16	0.02
Lailishan, Yunnan, China	LLS-Gr-1	74.8	93.2	34.2	17.4	0.54	0.17	0.03
	LLS-Gr-2	75.4	93.6	23.0	10.6	3.30	0.44	0.03
	LLS-Gr-3	77.5	97.0	10.9	24.9	0.35	0.26	0.08
Xiaolonghe, Yunnan, China	XLH-Gr-1	75.2	92.8	30.1	24.5	11.3	0.40	0.02
	XLH-Gr-1r	-	-	-	-	13.4	0.39	0.02
	XLH-Gr-2	75.2	93.4	32.1	27.3	20.5	0.24	0.02
	XLH-Gr-3	76.0	93.4	30.9	25.9	0.99	0.03	0.03
	XLH-Gr-4	76.2	92.7	24.7	22.6	0.87	0.70	0.03
	XLH-Gr-5	76.6	94.4	32.2	20.9	4.45	0.52	0.02
	XLH-Gr-6	76.3	94.3	32.7	20.6	3.04	0.40	0.03
	XLH-Gr-7	74.8	91.6	32.9	26.1	1.01	0.45	0.03
	XLH-Gr-8	75.9	93.2	30.1	24.2	0.67	0.14	0.03
Dasongpo, Yunnan, China	DSP-Gr-1	75.3	94.1	34.5	24.7	1.39	0.70	0.02
	DSP-Gr-2	75.0	94.1	35.5	25.7	2.58	0.83	0.03
	DSP-Gr-3	74.9	92.7	47.7	26.4	0.47	1.10	0.02
	DSP-Gr-4	74.9	93.4	30.5	25.8	2.38	0.73	0.03
	DSP-Gr-5	76.1	93.6	38.8	26.1	9.45	0.81	0.02
	DSP-Gr-6	75.2	93.9	39.0	26.4	2.04	0.61	0.03
	DSP-Gr-7	75.6	93.5	39.9	25.3	2.72	0.67	0.02

Discussion

Source-induced Mo isotope signature in tin granites

Tin is dominantly in the Sn^{4+} species under oxidized conditions and then dispersed in silicate minerals during magma differentiation, but it is dominantly in the Sn^{2+} species under reduced conditions and then enriched in residual magma by fractional crystallization (Lehmann 1982, 1987; Linnen et al. 1995, 1996). Therefore, sedimentary rocks such as shale with organic carbon are suitable magma sources of tin granites as they may imprint a low oxidation state (Ishihara 1977; Lehmann 1982; Sato et al. 2004). The genetic relationship between reduced sedimentary rocks and tin granites has been corroborated by various geochemical studies (e.g., Ishihara 1977, 1981; Mitchell and Garson 1981; Lehmann 1990; Romer and Kroner 2015, 2016; Yang et al. 2020).

A generally negative correlation between Re content and $\delta^{98}Mo$ in molybdenite from porphyry, epithermal, and iron-oxide Cu–Au deposits was recognized, suggesting

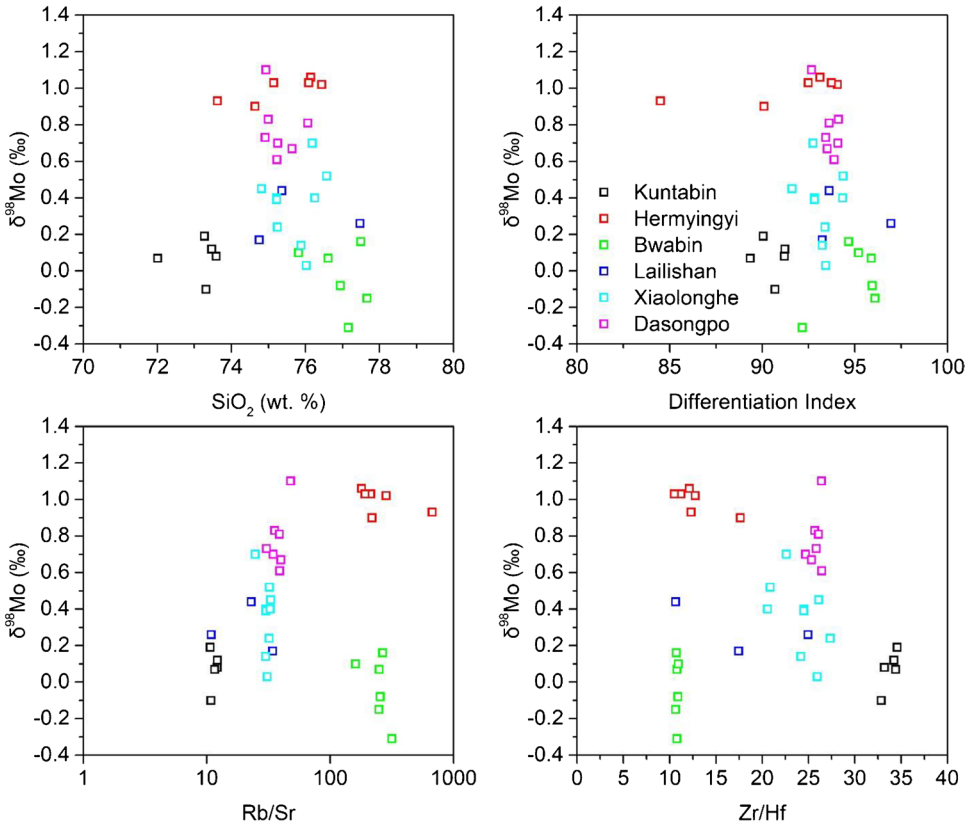

Fig. 3 Variations of δ^{98}Mo with SiO_2, Differentiation Index, Rb/Sr, and Zr/Hf of the studied tin granites

that magma sources controlled the Mo isotope signatures in these deposits (Mathur et al. 2010; Wang et al. 2015). Figure 5 shows that, besides several outliers, molybdenite from Sn–W deposits have lower Re contents and higher Mo isotope signatures than molybdenite from porphyry Cu–Mo deposits. Granites from the Kuntabin, Hermyingyi, and Bwabin deposits have very low zircon $\varepsilon_{Hf}(t)$ values of about −13 to −14 (ESM Table 1b; Mao et al. 2020). Granites from the Lailishan, Xiaolonghe, and Dasongpo deposits also have low zircon $\varepsilon_{Hf}(t)$ values of about -10 (Chen et al. 2015). The characteristically low oxygen fugacity of the studied tin granites (ESM Table 1a; Chen et al. 2015), $\varepsilon_{Hf}(t)$ values of zircon, and Re contents in molybdenite support the assumption that the studied tin granites were sourced from crust-derived reduced sedimentary rocks.

Mo isotope fractionation related to fractional crystallization is insignificant (compared to hydrothermal processes) in arc magma (Freymuth et al. 2015; König et al. 2016; Villalobos-Orchard et al. 2020), which can be attributed to the incompatibility of dominantly Mo^{6+} in oxic magma systems (Fig. 6A). Hydrous minerals (hornblende and biotite) have been inferred to selectively remove isotopically light Mo

Table 2 Mo contents in magmatic mica from granites in the Kuntabin, Hermyingyi, and Bwabin deposits

Deposits	Minerals	Percentage	Average Mo content (ppm)	Mo content ranges (ppm)	NO.
Kuntabin	Biotite	10%	0.25	0.05~0.61	30
	Muscovite	10%	0.32	0.10~0.55	30
Hermyingyi	Biotite	2%	0.31	0.01~0.61	10
	Muscovite	18%	0.16	0.04~0.44	35
Bwabin	Biotite	< 1 %	-	-	-
	Muscovite	15%	0.09	0.04~0.21	15

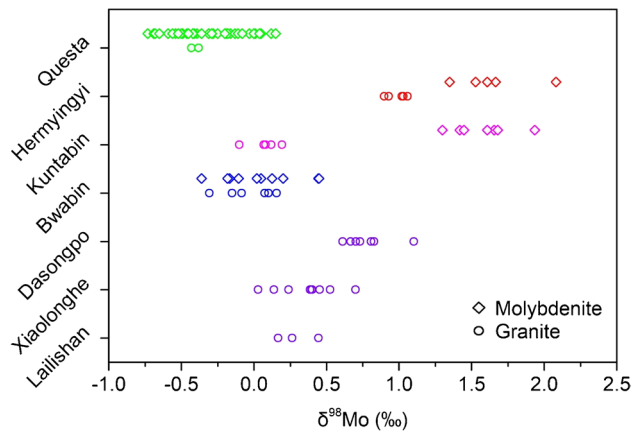

Fig. 4 δ^{98}Mo of granite and molybdenite from the studied Sn-W deposits. The Questa data are from Greber et al. (2014)

Table 3 δ^{98}Mo of molybdenite from the Kuntabin, Bwabin, and Hermyingyi deposits

Sample	$\delta^{98}Mo_{NIST}$ (‰)	2σ	Re content (ppm)
KTB-Mo-1	1.66	0.04	2.279
KTB-Mo-2	1.68	0.04	2.942
KTB-Mo-3	1.61	0.04	1.935
KTB-Mo-4	1.30	0.04	2.088
KTB-Mo-5	1.45	0.03	2.357
KTB-Mo-6	1.42	0.03	3.462
KTB-Mo-7	1.94	0.03	1.595
HMY-Mo-1	1.53	0.04	0.012
HMY-Mo-2	1.67	0.03	0.022
HMY-Mo-3	1.61	0.04	0.009
HMY-Mo-4	1.35	0.04	0.009
HMY-Mo-5	2.08	0.03	0.027
BB-Mo-1	-0.11	0.03	0.756
BB-Mo-2	-0.36	0.03	0.489
BB-Mo-3	0.13	0.03	0.180
BB-Mo-4	0.44	0.03	0.700
BB-Mo-5	0.20	0.03	0.328
BB-Mo-6	−0.17	0.04	0.647
BB-Mo-7	−0.18	0.03	0.801
BB-Mo-8	0.05	0.04	0.355
BB-Mo-9	0.02	0.03	1.214

and elevate the Mo isotope composition in the residual melt (Voegelin et al. 2014). However, fractional crystallization is not likely to have caused notable Mo isotopic fractionation in the studied tin granites because of the following: (1) Mo content in magmatic mica (avg. = 0.23 ppm) is over one order of magnitude lower than in the bulk granites (avg. = 3.4 ppm) in the studied deposits. The requirement of water saturation for mineralization contradicts the loss of a high proportion of hydrous minerals, so the fractionation of mica is not likely to remove significant amounts of Mo from the reduced melt. (2) Mo contents of the original reduced melts are not available, but the studied tin granites have notably higher Mo contents compared to the average Mo content of 1.5 ppm in sedimentary rocks (Taylor and McLennan 1995). (3) There are no systematic variations of δ^{98}Mo with the increase of SiO_2, Differentiation Index, Rb/Sr, or Zr/Hf values which demonstrate the extent of fractional crystallization of the studied tin granites (Fig. 3).

The Hermyingyi deposit is ~10 km to the northwest of the Bwabin deposit, and their ore-forming granites have similar zircon U-Pb ages (Fig. 1). The Dasongpo deposit is ~4 km to the northeast of the Xiaolonghe deposit, and both may belong to a large magmatic-hydrothermal system (Chen et al. 2014). The Hermyingyi and Bwabin granites have similar Rb/Sr and Zr/Hf values but distinctive Mo isotope compositions (Figs. 3C, D). A more notable feature is that the SiO_2, Differentiation Index, Rb/Sr, and Zr/Hf values cluster in very

Table 4 Summarized data of δ^{98}Mo and Mo contents in various Mo sinks

Sinks	δ^{98}Mo (‰)*	Mo content (ppm)	References
Riverwater	−0.10 ~ 2.15 (avg. = 0.58)	2 ~ 511** (avg. = 73)	Archer and Vance 2008
Seawater	2.09 ± 0.07	0.01	Greber et al. 2012
Arc lava	−0.19 ~ 0.38 (avg. = -−0.12; *n* = 186)	0.11 ~ 2.82 (avg. = 0.69)	Freymuth et al. 2015; König et al. 2016; Villalobos-Orchard et al. 2020; Ahmad et al. 2021; Li H.Y. et al. 2021a; Li X. et al. 2021b
Tin granites	−0.31 ~ 1.10 (avg. = 0.44; *n* = 36)	0.35 ~ 20.5 (avg. = 3.4)	This study
Porphyry Cu-Mo	−0.97 ~ 1.72 (avg. = −0.15; *n* = 244)	Molybdenite	Hannah et al. 2007; Mathur et al. 2010; Breillat et al. 2016; Segato 2018; Kong et al. 2021; Li et al. 2019a, 2019b; Chang et al. 2020 and references therein
Granite Sn-W	−0.36 ~ 2.08 (avg. = 0.92; *n* = 46)	Molybdenite	This study; Mao et al. 2013; Yao et al. 2016; Segato 2018 and references therein
Oxic sediments	−1.87 ~ 0.19 (avg. = −0.69; *n* =109)	0.05 ~ 902 (avg. = 192)	Nägler et al. 2005; Siebert et al. 2003; Brucker et al. 2009; Freymuth et al. 2015; Kendall et al. 2017 and references therein
Reduced sediments	−2.49 ~ 2.74 (avg. = 0.44; *n* =3348)	0.01 ~ 2103 (avg. = 29)	Scott and Lyons, 2012; Westermann et al. 2014; Goldberg et al. 2016; Dong et al. 2019; Ye et al. 2021 and references therein
Continental crust	0.05 ~ 0.15	0.8	Voegelin et al. 2014; Rudnick and Gao 2014
Depleted mantle	−0.21 ± 0.02	0.19	Bezard et al. 2016; Liang et al. 2017
MORB	−0.24 ~ -0.06 (avg. = −0.16; *n* = 28)	0.09 ~ 1.88 (avg. = 0.52)	Bezard et al.

*Normalized to $\delta^{98}Mo_{NIST3134}$=0

**Riverwater Mo content in nmol/L

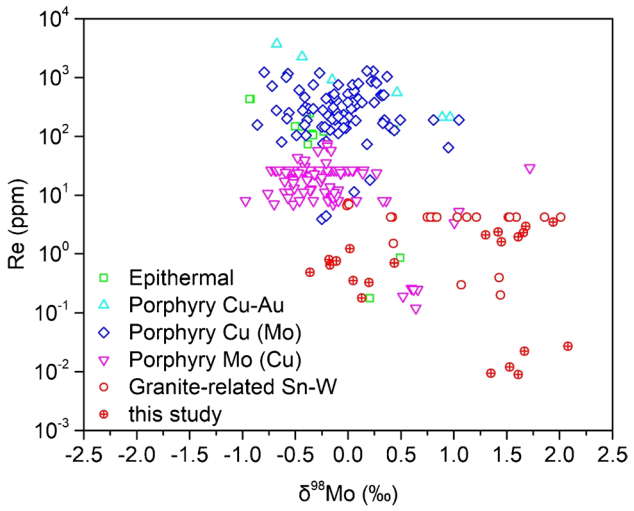

Fig. 5 Variations of δ^{98}Mo with Re contents of molybdenite from various types of deposits. See ESM Table 1c for data sources. All Mo isotope data have been re-calculated to δ^{98}Mo = 0 ‰ for NIST SRM 3134 for consistency

narrow ranges for the Xiaolonghe and Dasongpo granites, while their δ^{98}Mo varies significantly. Such patterns clearly demonstrate that fractional crystallization exerted no notable influence on the Mo isotope composition of the studied tin granites, and the variable δ^{98}Mo values in these deposits are likely inherited from their heterogeneous source material. The large variations of δ^{98}Mo in black shales and their average Mo isotope composition consistent with the studied tin granites support their genetic relationship and the lack of Mo isotope fractionation by fractional crystallization (Fig. 7; Table 4).

Magmatic-hydrothermal transition

The average Mo isotope composition of molybdenite from an individual deposit can be applied as an estimation of the Mo isotope signature of the input fluid (Hannah et al. 2007; Greber et al. 2011, 2014; Shafiei et al. 2014). We arbitrarily take the average Mo isotope values of granites in each deposit as the initial magma composition and define the fluid-melt fractionation of Mo isotopes as the difference of average Mo isotope values between molybdenite and granite. Then, the fluid-melt fractionation of Mo isotopes is minimal in the Questa porphyry Mo deposit (~0.09 ‰) and the Bwabin deposit (~0.05 ‰), but increases to ~0.65 ‰ in the Hermyingyi deposit and ~1.55 ‰ in the Kuntabin deposit (Fig. 4). Notably, the oxygen fugacity of the ore-forming magma decreases from >ΔFMQ+2 in Questa to ΔFMQ+0.1 in Bwabin to ΔFMQ-1.2 in Hermyingyi and ΔFMQ-2.3 in Kuntabin (ESM Table 1a).

Mo dissolves almost entirely as Mo^{6+} in silicate melts above the FMQ buffer, but the $Mo^{4+}/(Mo^{4+}+Mo^{6+})$ ratio increases to ~0.5 at the Iron-Wüstite buffer (around ΔFMQ-3.4; O'Neill and Eggins 2002). The slight fluid-melt fractionation of Mo isotopes in Questa and Bwabin can be attributed to differences in Mo^{6+} species between melt and hydrothermal fluid, as suggested by Greber et al. (2014). We infer that two additional mechanisms may have contributed to the elevated fluid-melt fractionation of Mo isotopes in Kuntabin and Hermyingyi where Mo^{4+} and Mo^{6+} coexist at the corresponding oxygen fugacity: (1) Dissolved Mo in aqueous fluids is dominantly Mo^{6+} at oxygen fugacity as low as ΔFMQ-0.8 (Zhang et al. 2012), so that Mo^{6+} and heavy Mo isotopes are preferentially partitioned into the exsolved

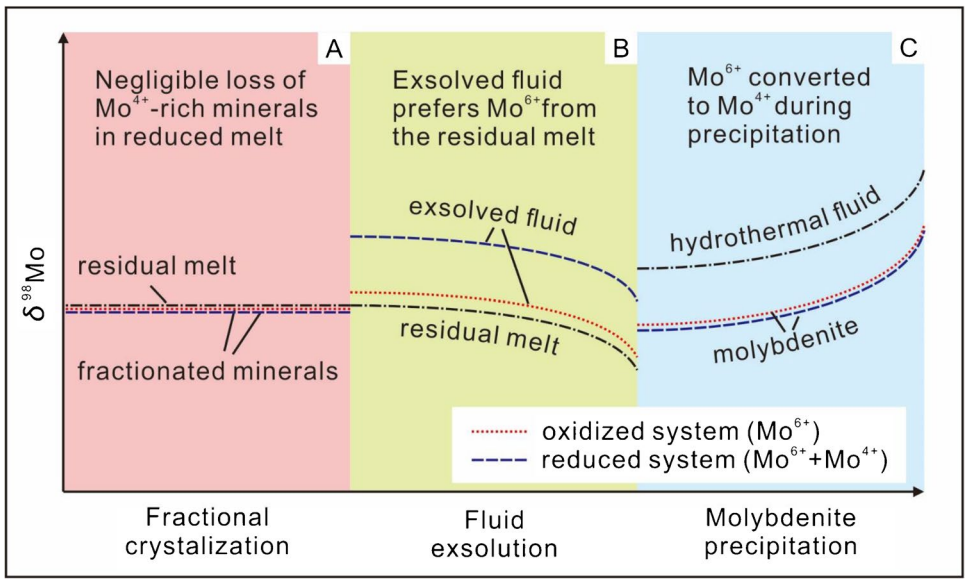

Fig. 6 Conceptual model for Mo isotope fractionation in oxic and reduced magmatic-hydrothermal systems

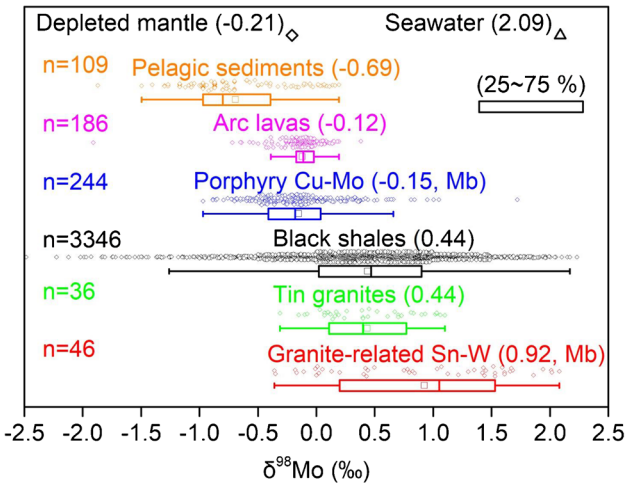

Fig. 7 Box-plot for the ranges of δ^{98}Mo in different Mo sinks. See Table 4 for data sources. Numbers in brackets are mean values in each group. Data for porphyry Cu–Mo deposits and granite-related Sn–W deposits refer to molybdenite (Mb) samples. All Mo isotope data have been re-calculated to δ^{98}Mo = 0 ‰ for NIST SRM 3134 for consistency

hydrothermal fluids (Kudrin 1989; Greber et al. 2014; Kaufmann et al. 2021). (2) The low content of Mo in magmatic mica compared to bulk granites suggests that magmatic sulfides are the dominant Mo reservoir in the studied granites, so that Mo^{4+} and isotopically light Mo are incorporated in magmatic sulfides during the magmatic-hydrothermal transition. Therefore, oxygen fugacity governs the extent of fluid-melt fractionation of Mo isotopes by controlling the Mo^{4+}/Mo^{6+} ratio (Fig. 6B).

Hydrothermal precipitation

Molybdenite precipitation from hydrothermal fluids may lead to significant kinetic Mo isotope fractionation (Hannah et al. 2007; Greber et al. 2011, 2014; Shafiei et al. 2014). $NaHMo(VI)O_2S_2$ and $Na_2Mo(VI)O_2S_2$ are the dominant Mo-bearing species in sulfur-bearing fluids at oxygen fugacity conditions as low as ΔFMQ-0.8 (Zhang et al. 2012). We assume that Mo in the hydrothermal fluid firstly experienced stoichiometric conversion from $MoO_2S_2^{-2}$ to MoS_4^{-2} during molybdenite precipitation in the studied Sn–W deposits (Erickson and Helz 2000), then the latter is converted to crystalline MoS_2. Tossell (2005) conducted ab initio calculations of isotope fractionation between $MoO_2S_2^{-2}$ and MoS_4^{-2} in the temperature range of 0 to 200°C. We extrapolated their data to 350°C, the typical temperature for greisen alteration (Little 1960; Heinrich 1990), and obtained the $\Delta^{98}Mo_{fluid\text{-}molybdenite}$ of ~1.02 ‰. The average Mo isotope composition of molybdenite from each deposit is used to represent the input Mo isotope signature (Hannah et al. 2007; Greber et al. 2011, 2014). The quantitative calculation revealed that the molybdenite samples in the studied deposits cover a very limited range of fractions of molybdenum in the residual fluid from ~23 to ~29 % (Fig. 8), indicating a notably lower precipitation efficiency than for the Yulong porphyry Cu–Mo deposit (>55 %, Chang et al. 2020). The general absence of coexisting vapor-rich fluid inclusions and halite-bearing fluid inclusions in the studied

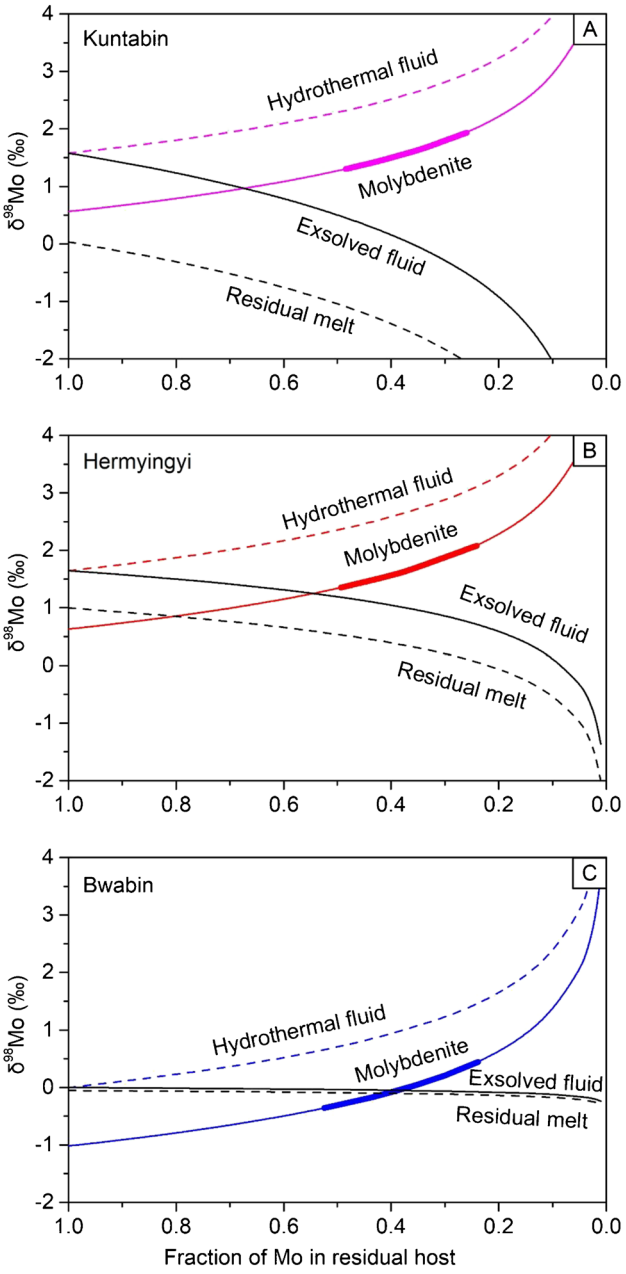

Fig. 8 Rayleigh fractionation of Mo isotopes during fluid exsolution from crystalizing melt and molybdenite precipitation from hydrothermal fluid for the Kuntabin and Hermyingyi magmatic-hydrothermal systems. Molybdenum isotope fractionation factors in the transitional stage are 1.00155 for Kuntabin, 1.00065 for Hermyingyi, and 1.00005 for Bwabin. Molybdenum isotope fractionation factor of 0.99898 was used for molybdenite precipitation from hydrothermal fluids. See text for detailed discussion

deposits indicates that fluid unmixing exerted no influence on Mo isotope fractionation in these systems.

Dual Mo cycling in Andean-type subduction

Andean-type subduction settings host two subparallel zones with contrasting magmatic and mineralization styles: the outer zone characterized by oxic arc magma and related porphyry Cu–Mo–Au deposits and the inner zone dominated by reduced magmatism and Sn–W mineralization (Sillitoe 1974; Clark et al. 1990). Figure 7 shows that the average Mo isotope composition of molybdenite in porphyry Cu–Mo deposits is consistent with the signature of arc lavas, but is notably heavier than for oxic sediments. In contrast, the average Mo isotope composition of tin granites is consistent with that of black shales but is notably lighter than molybdenite from granite-related Sn–W deposits. Below we propose a Mo cycling model in Andean-type subduction settings to address the Mo isotope composition patterns in different Mo sinks by multiple fractionation processes.

Notable Mo isotope fractionation (Δ) occurs by four processes during Mo cycling in the oxic arc system (Fig. 9). Δ_{O1} happens by adsorption of light Mo isotopes to Mn-oxides during the formation of pelagic sediments (Fig. 9; Barling et al. 2001; Siebert et al. 2003; Barling and Anbar 2004). Δ_{O2} happens by selective incorporation of light Mo isotopes into secondary minerals (e.g., rutile) and release of heavy Mo isotopes into dehydration fluids during slab subduction (Fig. 9; Bali et al. 2012; Freymuth et al. 2015; Skora et al. 2017; Chen et al. 2019; Ahmad et al. 2021; Li HY et al. 2021a). Δ_{O3} is caused by the difference of Mo^{6+} species between melt and hydrothermal fluid during fluid exsolution in porphyry systems (Greber et al. 2014). Δ_{O4} happens by preferential incorporation of light Mo isotopes during molybdenite precipitation from hydrothermal fluids (Hannah et al. 2007).

Black shales may record the Mo isotope composition of contemporaneous seawater if deposited under pervasively euxinic (anoxic and sulfidic) conditions (Barling et al. 2001; Arnold et al. 2004). However, Δ_{R1} occurs during non-quantitative removal of Mo in anoxic but non-euxinic or low $[H_2S]_{aq}$-seawater (Neubert et al. 2008; Gordon et al. 2009), leading to a very wide range of δ^{98}Mo in black shales (Fig. 7). Black shales deposited on continental margins can be cycled when the sedimentary crust is formed in extensional settings and melted by underplating in the back-arc setting of Andean-type subduction. There is no notable Mo isotope fractionation during fractional crystallization of the reduced magma, given the negligible loss of Mo-rich minerals. If reduced magma emplaced in the upper crust achieved water

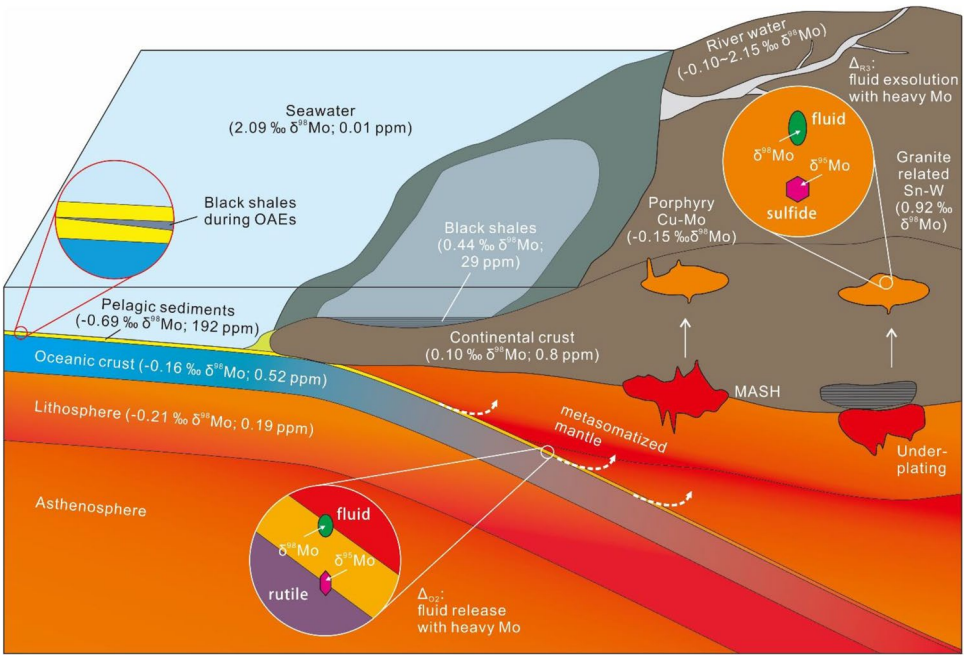

Fig. 9 Conceptual model for Mo cycling and isotope fractionation in Andean-type subduction settings. Mo in seawater is redistributed and isotopically fractionated during the formation of oxic and reduced sediments. Aqueous fluids released during slab dehydration extract heavy Mo isotopes (Δ_{O2}) from the oceanic slab. Hydrothermal fluids preferentially remove heavy Mo isotopes during exsolution from reduced melt (Δ_{R2}). See Table 4 for data sources. Note that Fe-Mn crusts have notably higher Mo contents (avg. = 445 ppm) and lower δ^{98}Mo (avg. = −0.96 ‰) compared to normal pelagic sediments (mean Mo content of 21 ppm and mean δ^{98}Mo of −0.54 ‰). Value for pelagic sediments in Figure 9 is the average of all available data in Table 4. MASH: Melting-Assimilation-Storage-Homogenization. OAEs: Oceanic Anoxic Events

saturation, the availability of Mo^{4+} to magmatic sulfides and Mo^{6+} to exsolving fluids facilitates the fractionation step Δ_{R2} between fluid and melt to produce hydrothermal fluids with elevated $\delta^{98}Mo$ (Figs. 6, 9; Kaufmann et al. 2021). During molybdenite precipitation in Sn-W deposits, Δ_{R3} happens by Rayleigh distillation which stretches the Mo isotope composition over a very wide range (Fig. 6C). The wide variation of $\delta^{98}Mo$ of molybdenite in granite-related Sn–W deposits can be explained by the following: (1) heterogeneous $\delta^{98}Mo$ of the reduced sedimentary sources with black shales; (2) variable Δ_{R2} related to different oxygen fugacity of the magmatic-hydrothermal systems; (3) kinetic fractionation of Mo isotopes during molybdenite precipitation (Δ_{R3}).

Conclusions

1. Black shales deposited on continental margins may be cycled by partial melting in the back-arc setting of Andean-type subduction by underplating of mafic melts, and there is no significant Mo isotope fractionation during fractional crystallization of the reduced magma. The heterogeneity and elevated signature of the Mo isotope composition in tin granites are inherited from their reduced sedimentary sources with black shales.
2. During the magmatic-hydrothermal transition, preferential incorporation of Mo^{4+} by magmatic sulfides and favored partitioning of Mo^{6+} into exsolved fluids both contribute to the fluid-melt fractionation of Mo isotopes, producing hydrothermal fluids with isotopically heavier Mo than in the reduced melt. Oxygen fugacity controls the ratio of Mo^{4+}/Mo^{6+} in silicate melt, and in turn, the transitional stage Mo isotope fractionation.
3. The sequestration of Mo during crystallization of reduced melt and low efficiency of Mo precipitation in the associated hydrothermal system prevents the formation of economic Mo mineralization in typical granite-related Sn-W deposits.

Supplementary Information The online version contains supplementary material available at https://doi.org/10.1007/s00126-023-01178-8.

Acknowledgements Constructive comments from Prof. Bernd Lehmann, Ryan Mathur, and an anonymous reviewer significantly improved this manuscript. We acknowledge the assistance from Dr. Kyaing Sein, Soe Myint Aung, and Ja Mu in the fieldwork. We thank Shengling Sun, Yezhi He, Junjie Han, and Defeng He for their assistance in the lab work.

Funding This work was financially supported by the National Natural Science Foundation of China (42121003, 42073045, 42073046), the K.C. Wong Education Foundation (GJTD-2020-13), and the Youth Innovation Promotion Association of the Chinese Academy of Sciences (NO. 2023416).

Declarations

Conflict of interest The authors declare no competing interests.

References

Ahmad Q, Wille M, König S, Rosca C, Hensel A, Pettke T, Hermann J (2021) The molybdenum isotope subduction recycling conundrum: a case study from the Tongan subduction zone, Western Alps and Alpine Corsica. Chem Geol 576. https://doi.org/10.1016/j.chemgeo.2021.120231

Anbar AD (2004) Molybdenum stable isotopes: observations, interpretations and directions. Rev Mineral Geochem 55:429–454

Archer C, Vance D (2008) The isotopic signature of the global riverine molybdenum flux and anoxia in the ancient oceans. Nat Geosci 1:597–600

Arnold GL, Anbar AD, Barling J, Lyons TW (2004) Molybdenum isotope evidence for widespread anoxia in Mid-Proterozoic oceans. Science 304:87–90

Bali E, Keppler H, Audetat A (2012) The mobility of W and Mo in subduction zone fluids and the Mo–W–Th–U systematics of island arc magmas. Earth Planet Sci Lett 351-352:195–207

Barling J, Anbar AD (2004) Molybdenum isotope fractionation during adsorption by manganese oxides. Earth Planet Sci Lett 217:315–329

Barling J, Arnold GL, Anbar AD (2001) Natural mass-dependent variations in the isotopic composition of molybdenum. Earth Planet Sci Lett 193:447–457

Bezard R, Fischer-Gödde M, Hamelin C, Brennecka GA, Kleine T (2016) The effects of magmatic processes and crustal recycling on the molybdenum stable isotopic composition of Mid-Ocean Ridge Basalts. Earth Planet Sci Lett 453:171–181

Breillat N, Guerrot C, Marcoux E, Négrel P (2016) A new global database of $\delta^{98}Mo$ in molybdenites: a literature review and new data. J Geochem Explor 161:1–15

Brucker RLP, McManus J, Severmann S, Berelson WM (2009) Molybdenum behavior during early diagenesis: insights from Mo isotopes. Geochem Geophys Geosyst 10:Q06010. https://doi.org/10.1029/2008GC002180

Chang J, Li JW, Zhou L (2020) Molybdenum isotopic fractionation in the Tibetan Yulong Cu-Mo deposit and its implications for mechanisms of molybdenite precipitation in porphyry ore systems. Ore Geol Rev 123. https://doi.org/10.1016/j.oregeorev.2020.103571

Chen S, Hin RC, John T, Brooker R, Bryan B, Niu Y, Elliott T (2019) Molybdenum systematics of subducted crust record reactive fluid flow from underlying slab serpentine dehydration. Nat Commun 10:4773

Chen XC, Hu RZ, Bi XW, Li HM, Lan JB, Zhao CH, Zhu JJ (2014) Cassiterite LA-MC-ICP-MS U/Pb and muscovite $^{40}Ar/^{39}Ar$ dating of tin deposits in the Tengchong-Lianghe tin district, NW Yunnan, China. Mineral Deposita 49:843–860

Chen XC, Hu RZ, Bi XW, Zhong H, Lan JB, Zhao CH, Zhu JJ (2015) Petrogenesis of metaluminous A-type granitoids in the Tengchong–Lianghe tin belt of southwestern China: Evidences from zircon U–Pb ages and Hf–O isotopes, and whole-rock Sr–Nd isotopes. Lithos 212-215:93–110

Clark AH, Farrar E, Kontak DJ, Langridge RJ, Arenas MJ, France LJ, McBride SL, Woodman PL, Wasteneys HA, Sandeman HA, Archibald DA (1990) Geologic and geochronologic constraints on the metallogenic evolution of the Andes of southeastern Peru. Econ Geol 85:1520–1583

Cobbing EJ, Mallic DIJ, Pitfield PEJ, Teoh LH (1986) The granites of the Southeast Asian tin belt. J Geol Soc Lond 143:537–550

Cong F, Wu FY, Li WC, Wang JG, Hu FY, He DF, Ji WQ, Lin W, Sein K (2021) Petrogenesis of the main range and eastern province granites in eastern Myanmar: new insights from zircon U-Pb ages and Sr–Nd isotopes. Lithos 105895:382–383

Ding L, Xu Q, Yue Y, Wang H, Cai F, Li S (2014) The Andean-type Gangdese Mountains: Paleoelevation record from the Paleocene–Eocene Linzhou Basin. Earth Planet Sci Lett 392:250–264

Dong B, Long X, Li J, Yang X, Zhao B, Luo J (2019) Mo isotopic variations of a Cambrian sedimentary profile in the Huangling area, South China: evidence for redox environment corresponding to the Cambrian Explosion. Gondwana Res 69:45–55

Erickson BE, Helz GR (2000) Molybdenum (VI) speciation in sulfidic waters: stability and lability of thiomolybdates. Geochim Cosmochim Acta 64:1149–1158

Freymuth H, Elliott T, Soes M, Skora S (2016) Tracing subducted black shales in the Lesser Antilles arc using molybdenum isotope ratios. Geology 44:987–990

Freymuth H, Vils F, Willbold MN, Taylor R, Elliott T (2015) Molybdenum mobility and isotopic fractionation during subduction at the Mariana arc. Earth Planet Sci Lett 432:176–186

Gardiner NJ, Robb LJ, Morley CK, Searle MP, Cawood PA, Whitehouse MJ, Kirkland CL, Roberts NMW, Myint TA (2016a) The tectonic and metallogenic framework of Myanmar: a Tethyan mineral system. Ore Geol Rev 79:26–45

Gardiner NJ, Searle MP, Morley CK, Whitehouse MP, Spencer CJ, Robb LJ (2016b) The closure of Palaeo-Tethys in Eastern Myanmar and Northern Thailand: new insights from zircon U–Pb and Hf isotope data. Gondwana Res 39:401–422

Gardiner NJ, Searle MP, Robb LJ, Morley CK (2015) Neo-Tethyan magmatism and metallogeny in Myanmar – an Andean analogue? J Asian Earth Sci 106:197–215

Goldberg T, Gordon G, Izon G, Archer C, Pearce CR, McManus J, Anbar AD, Rehkämper M (2013) Resolution of inter-laboratory discrepancies in Mo isotope data: an intercalibration. J Anal At Spectrom 28:724–735

Goldberg T, Poulton SW, Wagner T, Kolonic SF, Rehkämper M (2016) Molybdenum drawdown during Cretaceous Oceanic Anoxic Event 2. Earth Planet Sci Lett 440:81–91

Gordon GW, Lyons TW, Arnold GL, Roe J, Sageman BB, Anbar AD (2009) When do black shales tell molybdenum isotope tales? Geology 37:535–538

Greber ND, Hofmann BA, Voegelin AR, Villa IM, Nägler TF (2011) Mo isotope composition in Mo-rich high- and low-T hydrothermal systems from the Swiss Alps. Geochim Cosmochim Acta 75:6600–6609

Greber ND, Pettke T, Nägler TF (2014) Magmatic-hydrothermal molybdenum isotope fractionation and its relevance to the igneous crustal signature. Lithos 190-191:104–110

Greber ND, Siebert C, Nägler TF, Pettke T (2012) $\delta^{98/95}$Mo values and molybdenum concentration data for NIST SRM 610, 612 and 3134: towards a common protocol for reporting Mo data. Geostand Geoanal Res 36:291–300

Griffin WL, Wang X, Jackson SE, Pearson NJ, O'Reilly SY, Xu XS, Zhou XM (2002) Zircon chemistry and magma mixing, SE China: Insitu analysis of Hf isotopes, Tonglu and Pingtan igneous complexes. Lithos 61:237–269

Hannah JL, Stein HJ, Wieser ME, de Laeter JR, Varner MD (2007) Molybdenum isotope variations in molybdenite: vapor transport and Rayleigh fractionation of Mo. Geology 35:703–706

Heinrich CA (1990) The chemistry of hydrothermal tin(-tungsten) ore deposition. Econ Geol 85:457–481

Ishihara S (1977) The magnetite-series and ilmenite-series granitic rocks. Mining Geology 27:293–305

Ishihara S (1981) The granitoid series and mineralization. Economic Geology 75th Anniversary Volume, 458–484.

Ishihara S, Sawata H, Shibata K, Terashima S, Arrykul S, Sato K (1980) Granites and Sn-W deposits of peninsular Thailand: Mining. Geology Spec Issue 8:223–241

Jiménez N, López-Velásquez S (2008) Magmatism in the Huarina belt, Bolivia, and its geotectonic implications. Tectonophysics 459:85–106

Kaufmann AKC, Pettke T, Wille M (2021) Molybdenum isotope fractionation at upper-crustal magmatic-hydrothermal conditions. Chem Geol 578:120319

Kendall B, Creaser RA, Gordon GW and Anbar AD (2009) Re–Os and Mo isotope systematics of black shales from the Middle Proterozoic Velkerri and Wollogorang Formations, McArthur Basin, northern Australia. Geochimica et Cosmochimica Acta 73:2534–2558

Kendall B, Dahl TW, Anbar AD (2017) The stable isotope geochemistry of molybdenum. Rev Mineral Geochem 82:683–732

Kong DX, Cao K, Xu JF, Li J, Li W (2021) Molybdenum isotope systematics of subduction-related magmas from the Zhongdian region: assessing the Mo fractionation behavior in magmatic-hydrothermal processes. Ore Geol Rev 133. https://doi.org/10.1016/j.oregeorev.2021.104089

König S, Wille M, Voegelin A, Schoenberg R (2016) Molybdenum isotope systematics in subduction zones. Earth Planet Sci Lett 447:95–102

Kudrin AV (1989) Behavior of Mo in aqueous NaCl and KCl solutions at 300-450 °C. Geochem Int 26:87–99

Lehmann B (1982) Metallogeny of tin: magmatic differentiation versus geochemical heritage. Econ Geol 77:50–59

Lehmann B (1987) Tin granites, geochemical heritage, magmatic differentiation. Geol Rundsch 76:177–185

Lehmann B (1990) Metallogeny of Tin. Springer, Berlin Heidelberg, pp 1–211

Lehmann B (2021) Formation of tin ore deposits: a reassessment. Lithos 402-403, 105756. https://doi.org/10.1016/j.lithos.2020.105756

Lehmann B, Ishihara S, Michel H, Miller J, Rapela C, Sanchez A, Tistl M, Winkelmann L (1990) The Bolivian tin province and regional tin distribution in the Central Andes: a reassessment. Econ Geol 85:1044–1058

Lehmann B, Mahawat C (1989) Metallogeny of tin in central Thailand: A genetic concept. Geology 17:426–429

Li HY, Zhao RP, Li J, Tamura Y, Spencer C, Stern RJ, Ryan JG, Xu YG (2021a) Molybdenum isotopes unmask slab dehydration and melting beneath the Mariana arc. Nature. Communications 12:6015. https://doi.org/10.1038/s41467-021-26322-8

Li J, Liang XR, Zhong LF, Wang XC, Ren ZY, Sun SL, Zhang ZF, Xu JF (2014) Measurement of the isotopic composition of molybdenum in geological samples by MC-ICP-MS using a novel chromatographic extraction technique. Geostand Geoanal Res 38:345–354

Li JX, Fan WM, Zhang LY, Evans NJ, Sun YL, Ding L, Guan QY, Peng TP, Cai FL, Sein K (2019a) Geochronology, geochemistry and Sr–Nd–Hf isotopic compositions of Late Cretaceous–Eocene granites in southern Myanmar: Petrogenetic, tectonic and metallogenic implications. Ore Geol Rev 112. https://doi.org/10.1016/j.oregeorev.2019.103031

Li JX, Zhang LY, Fan WM, Ding L, Sun YL, Peng TP, Li GM, Sein K (2018) Mesozoic-Cenozoic tectonic evolution and metallogeny in Myanmar: Evidence from zircon/cassiterite U–Pb and molybdenite Re–Os geochronology. Ore Geol Rev 102:829–845

Li X, Yan Q, Zeng Z, Fan J, Li S, Li J, Yang H, Wang X (2021b) Across-arc variations in Mo isotopes and implications for subducted oceanic crust in the source of back-arc basin volcanic rocks. Geology 49:1165–1170

Li XH, Long WG, Li QL, Liu Y, Zheng YF, Yang YH, Chamberlain KR, Wan DF, Guo CH, Wang XC, Tao H (2010) Penglai zircon megacrysts: a potential new working reference material

for microbeam determination of Hf-O isotopes and U-Pb ages. Geostand Geoanal Res 34: 117–134.
Li Y, McCoy-West AJ, Zhang S, Selby D, Burton KW, Horan K (2019b) Controlling mechanisms for molybdenum isotope fractionation in porphyry deposits: the Qulong example. Econ Geol 114:981–992
Liang YH, Halliday AN, Siebert C, Fitton JG, Burton KW, Wang KL, Harvey J (2017) Molybdenum isotope fractionation in the mantle. Geochim Cosmochim Acta 199:91–111
Linnen RL, Pichavant M, Holtz F, Burgess S (1995) The effect of fO2 on the solubility, diffusion, and speciation of tin in haplogranitic melt at 850°C and 2 kbar. Geochimica et Cosmochimica Acta 59:1579–1588
Linnen RL, Pichavant M, Holtz F (1996) The combined effects of fO2 and melt composition on SnO2 solubility and tin diffusivity in haplogranitic melts. Geochimica et Cosmochimica Acta 60:4965–4976
Little W (1960) Inclusions in cassiterite and associated minerals. Econ Geol 55:485–509
Liu YS, Hu ZC, Gao S, Günther D, Xu J, Gao CG, Chen HH (2008) In situ analysis of major and trace elements of anhydrous minerals by LA-ICP-MS without applying an internal standard. Chem Geol 257:34–43
Liu YS, Hu ZC, Zong KQ, Gao CG, Gao S, Xu J, Chen HH (2010) Reappraisement and refinement of zircon U-Pb isotope and trace element analyses by LA-ICP-MS. Chin Sci Bull 55:1535–1546
Loucks RR, Fiorentini ML, Henríquez GJ (2020) New magmatic oxybarometer using trace elements. J Petrol 61:egaa034. https://doi.org/10.1093/petrology/egaa034
Lowell JD, Guilbert JM (1970) Lateral and vertical alteration-mineralization zoning in porphyry ore deposits. Econ Geol 65:373–408
Malinovsky D, Hammarlund D, Ilyashuk B, Martinsson O, Gelting J (2007) Variations in the isotopic composition of molybdenum in freshwater lake systems. Chem Geol 236:181–198
Mao W, Zhong H, Yang JH, Liu L, Fu YZ, Zhang XC, Tang YW, Li J, Zhang L, Sein K, Aung SM, Paw SMTL, Doh SH (2022) Geochronology of Sn mineralization in Myanmar: metallogenic implications. Econ Geol 117:1387–1403
Mao W, Zhong H, Yang JH, Tang YW, Liu L, Fu YZ, Zhang XC, Sein K, Aung SM, Li J, Zhang L (2020) Combined zircon, molybdenite, and cassiterite geochronology and cassiterite geochemistry of the Kuntabin tin-tungsten deposit in Myanmar. Econ Geol 115:603–625
Mao Z, Cheng Y, Liu J, Yuan S, Wu S, Xiang X, Luo X (2013) Geology and molybdenite Re-Os age of the Dahutang granite-related veinlets-disseminated tungsten ore field in the Jiangxi Province, China. Ore Geol Rev 53:422–433
Mathur R, Brantley S, Anbar A, Munizaga F, Maksaev V, Newberry R, Vervoort J, Hart G (2010) Variation of Mo isotopes from molybdenite in high-temperature hydrothermal ore deposits. Mineral Deposita 45:43–50
Mitchell AHG (1977) Tectonic settings for emplacement of Southeast Asian tin granites. Bulletin of the Geological Society of Malaysia 9:123–140
Mitchell AHG (1979) Rift-, subduction- and collision-related tin belts. Bulletin of the Geological Society of Malaysia 11:81–102
Mitchell AHG (1986) Mesozoic and Cenozoic regional tectonics and metallogenesis in Mainland SE Asia. Bulletin of the Geological Society of Malaysia 20:221–239
Mitchell AHG (1993) Cretaceous-Cenozoic tectonic events in the western Myanmar (Burma)-Assam region. J Geol Soc Lond 150:1809–1102
Mitchell AHG (2018) Geological belts, plate boundaries, and mineral deposits in Myanmar. Netherlands, Elsevier, Amsterdam, p 509
Mitchell AHG, Garson MS (1981) Mineral deposits and global tectonic settings. Academic Press, London, p 450
Mitchell AHG, Htay MT, Htun KM (2015) The medial Myanmar suture zone and the Western Myanmar-Mogok forland. Journal of Myanmar Geosciences Society 6:73–88
Nägler TF, Siebert C, Lüschen H, Böttcher ME (2005) Sedimentary Mo isotope record across the Holocene fresh–brackish water transition of the Black Sea. Chem Geol 219:283–295
Neubert N, Nägler TF, Böttcher ME (2008) Sulfidity controls molybdenum isotope fractionation into euxinic sediments: evidence from the modern Black Sea. Geology 36:775–778
O'Neill HSC, Eggins SM (2002) The effect of melt composition on trace element partitioning: an experimental investigation of the activity coefficients of FeO, NiO, CoO, MoO_2 and MoO_3 in silicate melts. Chem Geol 186:151–181
Qi L, Hu J, Gregoire DC (2000) Determination of trace elements in granites by inductively coupled plasma mass spectrometry. Talanta 51:507–513
Romer RL, Kroner U (2015) Sediment and weathering control on the distribution of Paleozoic magmatic tin–tungsten mineralization. Mineral Deposita 50:327–338
Romer RL, Kroner U (2016) Phanerozoic tin and tungsten mineralization—Tectonic controls on the distribution of enriched protoliths and heat sources for crustal melting. Gondwana Res 31:60–95
Royden LH, Burchfiel BC, Hilst RD (2008) The geological evolution of the Tibetan Plateau. Science 231:1054–1058
Rudnick RL, Gao S (2014) Composition of the Continental Crust. In: Holland HD, Turekian KK (eds) Treatise on Geochemistry 3. Elsevier, Amsterdam, pp 1–51
Sato K (2012) Sedimentary crust and metallogeny of granitoid affinity: implications from the geotectonic histories of the circum-Japan Sea Region, Central Andes and Southeastern Australia. Resour Geol 62:329–351
Sato K, Kovalenko SV, Romanovsky NP, Nedachi M, Berdnikov NV, Ishihara T (2004) Crustal control on the redox state of granitoid magmas: tectonic implications from the granitoid and metallogenic provinces in the circum-Japan Sea Region. Earth Environ Sci Trans R Soc Edinb 95:319–337
Schauble EA (2004) Applying stable isotope fractionation theory to new systems. Rev Mineral Geochem 55:65–111
Scherer E, Münker C, Mezger K (2001) Calibration of the lutetium-hafnium clock. Science 293:683–687
Schwartz MO, Rajah SS, Askury A, Putthapiban P, Djaswadi S (1995) The Southeast Asian Tin Belt. Earth Sci Rev 38:95–263
Scott C, Lyons TW (2012) Contrasting molybdenum cycling and isotopic properties in euxinic versus non-euxinic sediments and sedimentary rocks: Refining the paleoproxies. Chem Geol 324-325:19–27
Searle MP, Robb LJ, Gardiner NJ (2016) Tectonic processes and metallogeny along the Tethyan Mountain ranges of the Middle East and South Asia (Oman, Himalaya, Karakoram, Tibet, Myanmar, Thailand, Malaysia). Economic Geology Special Publication 19:301–327
Searle MP, Noble SR, Cottle JM, Waters DJ, Mitchell AHG, Hlaing T, Horstwood MSA (2007) Tectonic evolution of the Mogok metamorphic belt, Burma (Myanmar) constrained by U-Th-Pb dating of metamorphic and magmatic rocks. Tectonics 26. https://doi.org/10.1029/2006TC002083
Segato A (2018) Mo isotope variations in molybdenites at single-crystal, ore deposit, and global scales: Implications for Mo source fluid, transport, fractionation mechanisms, and molybdenite, PhD. Thesis. University of Waterloo, p 82
Shafiei B, Shamanian G, Mathur R, Mirnejad H (2014) Mo isotope fractionation during hydrothermal evolution of porphyry Cu systems. Mineral Deposita 50:281–291

Siebert C, Nägler TF, von Blanckenburg F, Kramers JD (2003) Molybdenum isotope records as a potential new proxy for paleoceanography. Earth Planet Sci Lett 211:159–171

Sillitoe RH (1973) The tops and bottoms of porphyry deposits. Econ Geol 68:799–815

Sillitoe RH (1974) Tectonic segmentation of the Andes: implications for magmatism and metallogeny. Nature 250:542–545

Sillitoe RH (2010) Porphyry copper systems. Econ Geol 105:3–41

Skora S, Freymuth H, Blundy J, Elliott T, Guillong M (2017) An experimental study of the behaviour of cerium/molybdenum ratios during subduction: Implications for tracing the slab component in the Lesser Antilles and Mariana Arc. Geochim Cosmochim Acta 212:133–155

Sone M, Metcalfe I (2008) Parallel Tethyan sutures in mainland Southeast Asia: new insights for Palaeo-Tethys closure and implications for the Indosinian orogeny. Compt Rendus Geosci 340:166–179

Taylor SR, McLennan SM (1995) The geochemical evolution of the continental crust. Rev Geophys 33:241–265

Thornton CP, Tuttle OF (1960) Chemistry of igneous rocks I. Differentiation index American Journal of Science 258:664–684

Tossell JA (2005) Calculating the partitioning of the isotopes of Mo between oxidic and sulfidic species in aqueous solution. Geochimica et Cosmochimica Acta 69:2981–2993

Tourtelot HA (1979) Black shale - Its deposition and diagenesis. Clays Clay Miner 27:313–321

Vervoort JD, Patchett PJ, Soderlund U, Baker M (2004) Isotopic composition of Yb and the determination of Lu concentrations and Lu/Hf by isotope dilution using MC-ICPMS. Geochem Geophys Geosyst 5:1–15

Villalobos-Orchard J, Freymuth H, O'Driscoll B, Elliott T, Williams H, Casalini M, Willbold M (2020) Molybdenum isotope ratios in Izu arc basalts: The control of subduction zone fluids on compositional variations in arc volcanic systems. Geochim Cosmochim Acta 288:68–82

Voegelin AR, Pettke T, Greber ND, von Niederhäusern B, Nägler TF (2014) Magma differentiation fractionates Mo isotope ratios: evidence from the Kos Plateau Tuff (Aegean Arc). Lithos 190-191:440–448

Wang Y, Zhou L, Gao S, Li JW, Hu ZF, Yang L, Hu ZC (2015) Variation of molybdenum isotopes in molybdenite from porphyry and vein Mo deposits in the Gangdese metallogenic belt, Tibetan Plateau and its implications. Mineral Deposita 51:201–210

Westermann S, Vance D, Cameron V, Archer C, Robinson SA (2014) Heterogeneous oxygenation states in the Atlantic and Tethys oceans during Oceanic Anoxic Event 2. Earth Planet Sci Lett 404:178–189

Willbold M, Hibbert K, Lai YJ, Freymuth H, Hin RC, Coath C, Vils F, Elliott T (2016) High-precision mass-dependent molybdenum isotope variations in magmatic rocks determined by double-spike MC-ICP-MS. Geostand Geoanal Res 40:389–403

Wu FY, Yang YH, Xie LW, Yang JH, Xu P (2006) Hf isotopic compositions of the standard zircons and baddeleyites used in U-Pb geochronology. Chem Geol 234:105–126

Yang J, Barling J, Siebert C, Fietzke J, Stephens E, Halliday AN (2017) The molybdenum isotopic compositions of I-, S- and A-type granitic suites. Geochim Cosmochim Acta 205:168–186

Yang J, Siebert C, Barling J, Savage P, Liang YH, Halliday AN (2015) Absence of molybdenum isotope fractionation during magmatic differentiation at Hekla volcano, Iceland. Geochim Cosmochim Acta 162:126–136

Yang JH, Zhou MF, Hu RZ, Zhong H, Williams-Jones AE, Liu L, Zhang XC, Fu YZ, Mao W (2020) Granite-related tin metallogenic events and key controlling factors in Peninsular Malaysia, Southeast Asia: new insights from cassiterite U-Pb dating and zircon geochemistry. Econ Geol 115:581–601

Yao JM, Mathur R, Sun WD, Song WL, Chen HY, Mutti L, Xiang XK, Luo XH (2016) Fractionation of Cu and Mo isotopes caused by vapor-liquid partitioning, evidence from the Dahutang W-Cu-Mo ore field. Geochem Geophys Geosyst 17:1725–1739

Ye Y, Zhang S, Wang H, Wang X, Tan C, Li M, Wu C, Canfield DE (2021) Black shale Mo isotope record reveals dynamic ocean redox during the Mesoproterozoic Era. Geochemical Perspectives Letters 18:16–21

Zhang L, Audétat A, Dolejš D (2012) Solubility of molybdenite (MoS_2) in aqueous fluids at 600–800°C 200 MPa: a synthetic fluid inclusion study. Geochim Cosmochim Acta 77:175–185

Zhang Q, Zhao KD, Li WQ, Palmer MR, Jiang SY, Jiang H, Zhang W, Zhang D, Hussain A (2021) Timing and tectonic setting of tin mineralization in southern Myanmar: constraints from cassiterite and wolframite U–Pb ages. Mineralium Deposita. https://doi.org/10.1007/s00126-021-01083-y

Zhao PL, Chu X, Williams-Jones AE, Mao JW, Yuan SD (2022) The role of phyllosilicate partial melting in segregating tungsten and tin deposits in W-Sn metallogenic provinces. Geology 50:121–125